Proceedings of the ASME 2023
International Mechanical Engineering Congress and Exposition
IMECE2023
October 29–November 2, 2023, New Orleans, LA

IMECE2023-110906

NUMERICAL STUDY OF LIQUID PISTON COMPRESSION USING LARGE-EDDY SIMULATION AND VOLUME-OF-FLUID APPROACH

Thien D.Nguyen[1,*], Joe Rendall[1], Steve Kowalski[1],

[1]Oak Ridge National Laboratory, Oak Ridge, Tennessee, USA.

ABSTRACT

In the United States, residential and commercial heating and cooling use 4.4 Quads of primary energy and are responsible for 148 Mt of CO_2 emissions annually (DOE, 2018). Efforts to increase the efficiency of residential and commercial air conditioners and heat pumps have demonstrated that the compressor accounts for most of the system's electrical energy usage. Therefore, the efficiency of this component should be improved to reduce its energy usage. The US Department of Energy's Oak Ridge National Laboratory developed a near-isothermal liquid piston compressor that uses propylene glycol (PG) to compress CO_2. This report presents numerical studies of the liquid piston compressor in which the compression chamber fills with injected PG from the bottom inlet. Numerical simulations were performed using the large-eddy simulation (LES) with the wall-adapting local eddy-viscosity (WALE) subgrid-scale model coupled with the multiphase volume-of-fluid (VOF) model to simulate the transient interface between gas and liquid and to capture the heat and mass transfer within the compression chamber. In this effort, effects of boundary conditions applied to the LES-VOF calculations (e.g., no wall, an adiabatic wall, and a wall with a heat flux subscribed) to the overall pressure and temperature of CO_2 gas as well as the transient evolution of flow and heat transfer evolution within the compression chamber are investigated and discussed.

Keywords: Liquid compressor, heat pump, computational fluid dynamics, large-eddy simulation, volume of fluid.

1. INTRODUCTION

In the United States, residential and commercial heating and cooling use 4.4 Quads of primary energy and are responsible for 148 Mt of CO_2 emissions annually. Extensive efforts have been attempted to increase the efficiency of residency and commercial air conditioners and heat pumps. Conventional compressors in vapor compression cycles work to increase the pressure and saturation temperature of coolant fluid (refrigerant) to those required in the condenser. The current compression process is performed at a high speed, allowing only very short duration for coolant gas to exchange heat with its surroundings. This process yields huge viscous dissipation and high discharge temperatures. For cooling devices based on compressing vapor, superheated coolant rejects heat to the surroundings in the condenser. Because the conventional heat exchangers used refrigerant-air has low overall heat transfer coefficients, numerous attempts have been made to improve their efficiencies. For instance, increasing the approach temperature difference would increase the compressor lift and eventually reduce the efficiency of the compressor and refrigeration cycle. Furthermore, conventional heat pump compressors cannot compress two-phase refrigerants because of pitting damage caused by wet vapors. This limitation hinders the maximum achievable coefficient of performance (COP) of a vapor compression cycle as it departs from the ideal Carnot limit.

To address these challenges, the US Department of Energy's Oak Ridge National Laboratory developed a near-isothermal liquid compressor that uses propylene glycol (PG) to compress CO_2. In the current design, liquid PG can enter the compression chamber in two ways: (1) from the bottom inlet to create a liquid piston for compression and (2) from the spray nozzle at the top of the chamber. In the former case, the liquid piston compressor offers a major advantage compared with a traditional solid piston to avoid gas leakage and reduce dissipation owing to friction, yielding an overall higher efficiency [1, 2].

Several studies have examined the use of sprayed droplets and similar concepts for achieving isothermal compression. Gerstmann and Hill [3] provided an analytical study of increasing the

*Corresponding author: nguyend@ornl.gov

efficiency of a refrigeration process by isothermalization of compression. In that work, the refrigerant was cooled by an aerosol that was externally cooled. The aerosol then became the liquid piston that compressed the refrigerant. The authors noted that for the aerosol, the droplets and the surface area must be small to transfer the heat stored in the liquid to the working gas. Van de Ven et al. [1] created a computer model of a liquid piston concept designed to improve the efficiency of gas compression and expansion and found that greater efficiency could be achieved by using a larger quantity of small-diameter compression cylinders, improving the heat transfer while minimizing the viscous flow forces. Although the study did not specifically involve droplet spray heat transfer, several items were noted as necessary for successful liquid piston compression. First, a portion of the gas will diffuse in the liquid, possibly reducing the liquid's bulk modulus. This change can be avoided by designing the chamber to minimize liquid splashing, by selecting a fluid with low gas solubility, or by using a bladder to physically separate the liquid and the gas. Furthermore, the liquid should not be allowed to leave the compression chamber during the gas exhaust stroke.

The concept of compression cooling via liquid droplets has also been applied to compressed air energy storage (CAES). One of the main challenges of conventional CAES systems is the increase/decrease of air temperatures during the compression/expansion processes, resulting in a low round-trip efficiency. Attempts have been made to develop a new CAES technology to achieve near-isothermal operations via efficient thermal management of heat release and supply [4, 5]. The concept of a liquid piston compressor has been investigated [1] and compared with conventional solid piston design: a reduction of 19% energy consumption and an increase of 13% compression efficiency were achieved when using the liquid piston compressor.

Qin et al. [6, 7] performed numerical simulations of a liquid piston compressor using droplets and reported that the droplets' total surface area was the most important characteristic for increasing compression efficiency. These authors also found that small droplets and high mass loading—defined as the ratio of the mass of water injected into the chamber to the mass of air already in the chamber—were optimal, which agrees with the conclusions of Gerstmann and Hill [3].

Odukomaia et al. [8] performed computer modeling and experiments to study spray cooling to improve the round-trip efficiency of a hydropneumatic energy storage system using a liquid piston compressor and direct-contact heat exchanger for waste heat recovery. The researchers found that both spray cooling during compression and waste heat utilization during expansion provided improved efficiency. Indicated efficiency—defined by the researchers as the work output divided by the work input—which only includes the thermodynamic losses, increased from 0.90 to 0.96, whereas the electrical efficiency, which includes all loses, increased from 0.66 to 0.70.

In a study of the compression of air using a water piston [9], Patil et al. used a compression ratio of approximately 2.5 at injection pressures varying from 10 to 70 psi (69 to 483 kPa) and spray angles of 60°, 90°, and 120°. They defined isothermal efficiency to express how closely the compression process follows an isothermal trajectory and attributed the wide spray angle's reduced efficiency to the droplets colliding with the walls of the chamber, rendering them unavailable to participate in heat transfer.

Studies from Segula Technologies [10] and Oak Ridge National Laboratory's Ground-Level Integrated Diverse Energy Storage project [8] reported significantly improved efficiency (up to 95%) for the compression and expansion processes obtained by using the liquid piston technology. Although many experimental and numerical studies have been performed to acquire characteristics of the compression and expansion processes featuring the liquid piston technology, most studies presented the evolution of global temperature and pressure within the gas volume. The obtained results were then later used to develop and improve heat transfer models and to compute the round-trip efficiency. Only a few studies aimed to characterize the thermal fluid phenomena that occurred within the compression chamber. Most numerical studies on liquid piston compressors were performed on a 2D domain to reduce the high computational cost compared with 3D simulations.

Zhang et al. [11, 12] performed 2D numerical simulations of an air compressor using water and found that a lower heat transfer rate and lower compression efficiency were caused by high liquid injection rate and high piston velocity. A higher Reynolds number at high piston speed would cause the lower heat-transfer rate during the compression process and thus the lower compression efficiency. Similar findings were also discussed in the 2D numerical study featuring a moving boundary of a solid piston [13].

Gouda et al. [5] discussed that the spatial simplifications applied in 2D simulations have limited the capability to correctly capture the complex and dynamically evolving thermo-hydrodynamic behaviors of the gas flow within the compressor volume. The authors argued that the flow patterns within the chamber possess the 3D nature of flow structures and local turbulence that cannot be simulated in 2D calculations. Furthermore, Shah et al. [14] discussed that the 2D simulations had doubled the compactness ratio compared with 3D geometry and underestimated the heat exchange between the wall and fluids inside the chamber, further altering the gas flow patterns. Therefore, 3D numerical simulations of liquid piston compressor are necessary to characterize the thermo-hydrodynamic behaviors within the compression chamber [5, 15, 16].

This study presents numerical studies of a liquid piston compressor in which the chamber fills with liquid PG from the bottom inlet to compress CO_2. Numerical simulations were performed using LES coupled with the multiphase VOF model to simulate the transient interface between liquid PG and CO_2 gas and to capture the heat and mass transfer within the volume of the compression chamber. In the present work, the wall-adapting local eddy-viscosity (WALE) subgrid-scale (SGS) model featuring a novel form of the velocity gradient tensor in its formulation was applied because of its advantages over the Smagorinsky model. The VOF model is suitable for model flows involving immiscible fluids, fluid mixtures, free surfaces, and phase contact on numerical grids capable of resolving the interface between the phases. In this effort, effects of boundary conditions applied to the CFD-VOF calculations (e.g., no wall, an adiabatic wall,

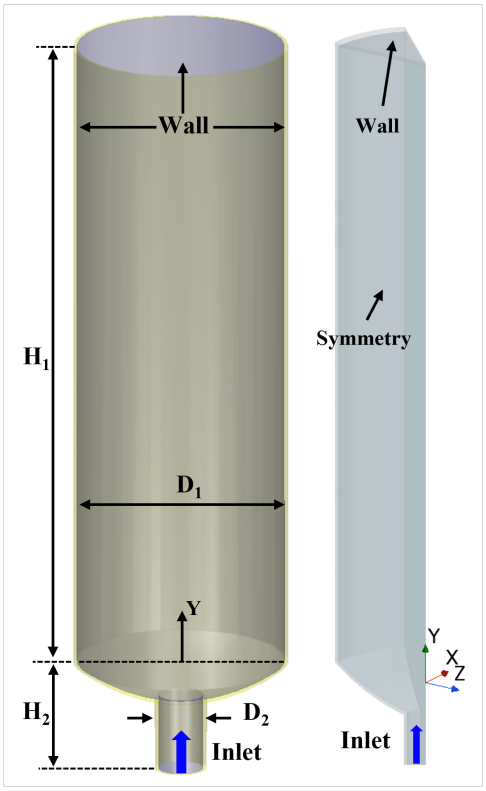

FIGURE 1: (LEFT) DESIGN OF A LIQUID PISTON COMPRESSOR, (RIGHT) COMPUTATIONAL DOMAIN USED IN THIS STUDY.

and a thick wall with a heat flux subcribed) to the overall pressure and temperature as well as the transient evolutions of flow and heat transfer evolution within the compression chamber are investigated and discussed. Results from this work will elucidate the entire cycle of compression and expansion in the liquid piston design and will be used to improve the physics-based thermodynamic model used for the system design and evaluation of near-isothermal compressed-gas energy storage. Moreover, the numerical results of the LES-VOF model will support the development of a second-generation prototype in which more rapid cycling is possible.

2. NUMERICAL SIMULATION OF A LIQUID PISTON COMPRESSOR

2.1 Numerical domain

Figure 1(left) shows the configuration of the liquid piston compressor in which the chamber fills from the bottom inlet that was considered in this study. The compressor had a total height of 323.6 mm and consisted of a cylindrical chamber with a vertical length of $H_1 = 275.34$ mm and an internal diameter of $D_1 = 88.9$ mm. The inlet nozzle had an internal diameter of $D_2 = 19.05$ mm. The x- and z-coordinates represented the horizontal planes, and the y-coordinate denoted the vertical direction. The origin of the coordinate system was the center of the chamber at the distance of $H_2 = 48.26$ mm from the nozzle inlet. The compression chamber was designed to allow CO_2 to enter from the top and the compression fluid (i.e., liquid PG) to enter from the nozzle inlet at the bottom.

In this study, the internal volume of the chamber is initially occupied by CO_2 gas, and the compression process starts when liquid PG is injected into the chamber bottom via the nozzle inlet with mass flow rate of $Q_1 = 2$ L/min. Initial conditions of the chamber were at a temperature of 305 K, a pressure of 2 MPa, and the liquid PG level at the origin $y = 0$. The compression process stops when the chamber's internal pressure reaches 8.6 MPa. In this study, to reduce the computational cost, the numerical domain of the compressing chamber was reproduced with a 45° angle portion with two cutting surfaces were considered as symmetry planes as shown in Figure 1(right). The thermal fluid flow phenomena within the chamber volume during the compression process are expected to be complex, involving unsteady compressible multiphase flow physics of liquid and gas associated with conjugated heat transfer. During the compression process, liquid PG was injected into the chamber at a constant mass flow rate such that the liquid velocity could be considered a constant. The CO_2 gas within the chamber volume is compressed, making the gas flow patterns dynamically evolve and very complex. The CO_2 gas temperature during the compression will increase, inducing heat transfer between the gas and liquid at their interfaces. Furthermore, convection heat transfer will occur among the gas, liquid, and chamber wall, depending on the spatial location of the gas–liquid interface, the gas flow patterns, the thermal resistance of the wall, and the ambient temperature. The chamber wall was specified by a no-slip boundary. In this study, numerical calculations were performed considering several boundary conditions of the chamber wall, including no-wall (only the interior volume of chamber), a wall with a constant temperature, and a wall with a constant heat flux. These considerations allowed for investigating the interactions between the solid wall and the flow inside the chamber during the compression process.

2.2 Numerical modeling

Applying the considerations suggested in previous studies [5, 16], the following assumptions were made in the numerical modeling of liquid compressor in this study. The ideal gas law was applied for the gas phase (CO_2) with a specific heat of $C_p = 1020.6$ J/kg·K, a thermal conductivity of $\lambda_g = 0.018153$ W/m·K, and a molecular weight of 44.01 kg/kmol. The Sutherland equation (Eq. 1) was applied for the temperature-dependent viscosity of CO_2:

$$\mu(T) = \mu \frac{T_0 + C}{T + C} \left(\frac{T}{T_0}\right)^{3/2}, \tag{1}$$

where the Sutherland coefficient $C = 110.4$, the reference temperature $T_0 = 273.15$ K, and the reference viscosity $\mu_0 = 1.716 \times 10^{-5}$ Pa·s. The liquid phase (PG) is considered incompressible flow with a density of $\rho_l = 1048$ kg/m^3, a dynamic viscosity of $\mu_l = 0.056$ Pa·s, a specific heat of $C_p = 3251$ J/kg·K, a thermal conductivity of $\lambda_g = 0.223$ W/m·K, and a molecular weight of 76.1 kg/kmol. No phase change occurred for the working fluids, and no mass transfer occurred between the liquid and gas phases.

In this study, numerical simulations of a liquid piston compressor were performed using the LES coupled with the multiphase VOF model to simulate the transient interface between

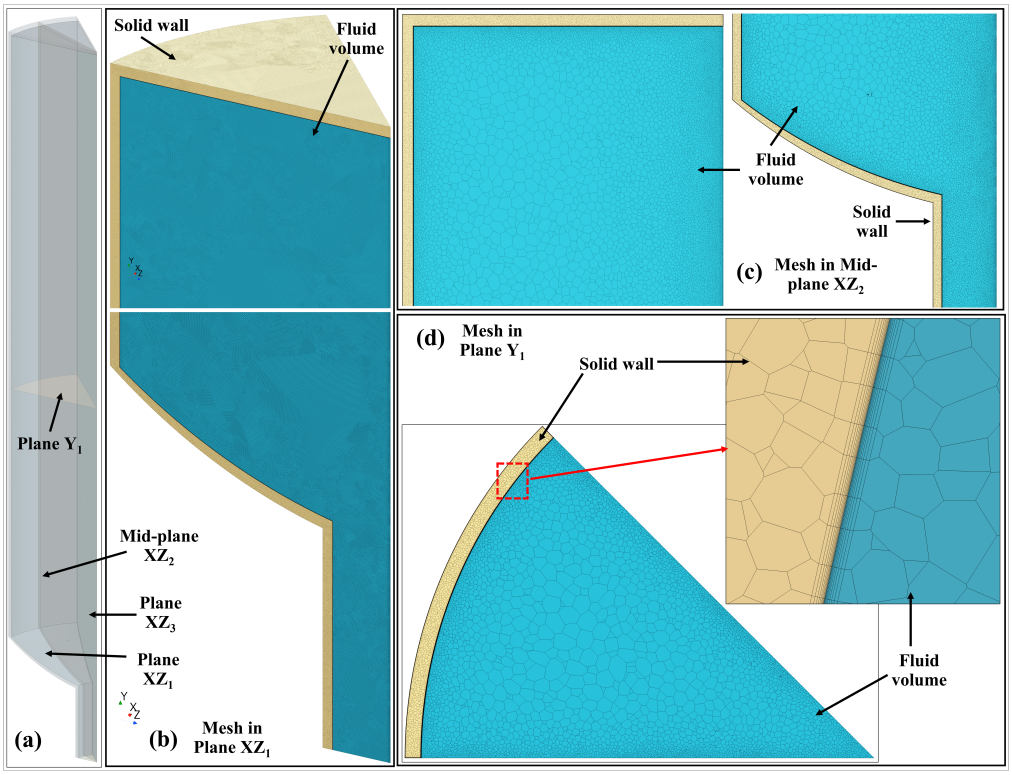

FIGURE 2: (a) COMPUTATIONAL DOMAIN WITH VERTICAL PLANES XZ_0, MID-PLANES XZ_2 AND XZ_3, AND HORIZONTAL PLANE Y_1. COMPUTATIONAL MESH GENERATED IN THE SOLID WALL (YELLOW) AND FLUID REGION (GREEN) USED IN THIS STUDY, (b) MESH IN PLANE XZ_1, (c) MESH IN MID-PLANE XZ_2, AND (d) MESH IN PLANE Y_1.

liquid PG and CO_2 gas and to capture the heat and mass transfer within the volume of the compression chamber. The WALE SGS model featuring a novel form of the velocity gradient tensor in its formulation was applied in the present work because of its advantages over the Smagorinsky model. In a previous study of a liquid piston compressor [5], the performances of LES Smagorinsky and WALE sub-grid models were compared, and the WALE model managed the flow transition and more accurately captured the near-wall region. The VOF model was selected because it is suitable for model flows involving immiscible fluids, fluid mixtures, free surfaces, and phase contact on numerical grids capable of resolving the interface between the phases [17].

The turbulent fluid motion is governed by conservation of mass, linear momentum, and energy, given as follows:

$$\frac{\partial \rho}{\partial t} + \nabla \cdot (\rho \boldsymbol{v}) = 0, \tag{2}$$

where ρ is the density, and v is the continuum velocity.

$$\frac{\partial (\rho \boldsymbol{v})}{\partial t} + \nabla \cdot (\rho \boldsymbol{v} \otimes \boldsymbol{v}) = -\nabla \cdot (p\boldsymbol{I}) + \nabla \cdot \boldsymbol{T} + \boldsymbol{f}_b, \tag{3}$$

where $\otimes$ denotes the outer product, f_b is the resultant of the body forces per unit volume acting on the continuum, and σ is the stress tensor. For a fluid, the stress tensor is often written as the sum of normal stresses and shear stresses, $\sigma = -pI + T$, where p is the pressure, and T is the viscous stress tensor.

$$\frac{\partial (\rho E)}{\partial t} + \nabla \cdot (\rho E \boldsymbol{v}) = \boldsymbol{f}_b \cdot \boldsymbol{v} + \nabla \cdot (\boldsymbol{v} \cdot \boldsymbol{\sigma}) - \nabla \cdot \boldsymbol{q} + \boldsymbol{S}_E, \tag{4}$$

where E is the total energy per unit mass, q is the heat flux, and S_E is an energy source per unit volume.

An LES resolves turbulent structures in space everywhere in the flow domain down to the grid limit, whereas subgrid models approximate the effect of the subgrid structures on the flow field. To resolve the crucial turbulent structures near the wall, this approach requires an excessively high mesh resolution in the wall boundary layer—not only in the direction normal to the wall but also in the flow direction. LES is an inherently transient technique in which the large scales of the turbulence depend on the geometry and are directly resolved everywhere in the flow domain, whereas the small-scale motions (eddies) behave universally and are modeled [18]. The large-scale motions are resolved by the filtered Navier–Stokes equation, and the small-scale motions are modeled by SGS models. The governing equations for LES are derived by spatially filtering the time-dependent three-dimensional Navier-Stokes equations. Each solution variable ϕ is decomposed into a filtered value $\tilde{\phi}$ and a subfiltered, or subgrid, value ϕ' as follows:

$$\phi = \tilde{\phi} + \phi', \tag{5}$$

where ϕ represents velocity components, pressure, energy, or species concentration. The spatial filtering removes the smaller eddies—associated with higher frequencies—and thereby reduces the range of scales that must be resolved. LES filtering can be either explicit or implicit. Explicit filtering applies a filter function (such as box or Gaussian) to the discretized Navier–Stokes equations. The filtering of the generic instantaneous flow

variable $\phi(t,x)$ is defined as follows:

$$\tilde{\phi}(t,x) = \iiint_{-\infty}^{\infty} G(x-x',\Delta)\phi(t,x')dx', \tag{6}$$

where $G(x,\Delta)$ is the filter function characterized by a filter width $\Delta = \left(\Delta_x\Delta_y\Delta_z\right)^{1/3}$. For this approach, the computational grid determines the scales of the eddies that are filtered out. Inserting the decomposed solution variables into the Navier–Stokes equations yields equations for the filtered quantities. The filtered mass, momentum, and energy transport equations can be written as follows:

$$\frac{\partial \rho}{\partial t} + \nabla \cdot (\rho \tilde{\boldsymbol{v}}) = 0, \tag{7}$$

$$\frac{\partial}{\partial t}(\rho\tilde{\boldsymbol{v}}) + \nabla \cdot (\rho\tilde{\boldsymbol{v}} \otimes \tilde{\boldsymbol{v}}) = -\nabla \cdot (\tilde{p}I) + \nabla \cdot \left(\tilde{\boldsymbol{T}} + \boldsymbol{T}_{SGS}\right) + \boldsymbol{f}_b, \tag{8}$$

$$\frac{\partial}{\partial t}\left(\rho\tilde{E}\right) + \nabla\cdot(\rho\tilde{E}\tilde{\boldsymbol{v}}) = -\nabla\cdot\tilde{p}\tilde{\boldsymbol{v}} + \nabla\cdot\left(\tilde{\boldsymbol{T}} + \boldsymbol{T}_{SGS}\right)\tilde{\boldsymbol{v}} - \nabla\cdot\tilde{\boldsymbol{q}} + \boldsymbol{f}_b\tilde{\boldsymbol{v}}, \tag{9}$$

where $\tilde{\boldsymbol{v}}$ is the filtered velocity, $\tilde{p}$ is the filtered pressure, $\boldsymbol{I}$ is the identity tensor, $\tilde{\boldsymbol{T}}$ is the filtered stress tensor, $\tilde{E}$ is the filtered total energy per unit mass, and $\tilde{\boldsymbol{q}}$ is the filtered heat flux. These stresses result from the interaction between the larger, resolved eddies and the smaller, unresolved eddies and are modeled using the Boussinesq approximation as follows:

$$\boldsymbol{T}_{SGS} = 2\mu_t\boldsymbol{S} - \frac{2}{3}\left(\mu_t\nabla\cdot\tilde{\boldsymbol{v}}\right)\boldsymbol{I}, \tag{10}$$

where $\boldsymbol{S}$ is the strain rate tensor and is computed from the resolved velocity field $\tilde{\boldsymbol{v}}$. The mean strain rate tensor $\boldsymbol{S}$ is given by

$$\boldsymbol{S} = \frac{1}{2}\left(\nabla\bar{\boldsymbol{v}} + \nabla\bar{\boldsymbol{v}}^T\right), \tag{11}$$

where $\boldsymbol{v}$ is the mean velocity. The SGS turbulent viscosity μ_t must be described by an SGS model that accounts for the effects of small eddies on the resolved flow. This study employed a WALE SGS model featuring a novel form of the velocity gradient tensor in its formulation. The WALE SGS model [19] provides the following mixing-length type formula for the SGS viscosity:

$$\mu_t = \rho\triangle^2 S_w, \tag{12}$$

where $\triangle$ is the length scale or grid filter width, and S_w is a deformation parameter. The length scale $\triangle$ is defined in terms of the cell volume V:

$$\triangle = \begin{cases} C_w V^{1/3}, & \text{if length scale limit is not applied} \\ min\left(\kappa d, C_w V^{1/3}\right), & \text{if length scale limit is applied,} \end{cases} \tag{13}$$

where C_w is a model coefficient, and κ is the von Karman constant. The deformation parameter S_w is defined as follows:

$$S_w = \frac{\boldsymbol{S}_d : \boldsymbol{S}_d^{3/2}}{\boldsymbol{S}_d : \boldsymbol{S}_d^{5/4} + \boldsymbol{S} : \boldsymbol{S}^{5/2}}. \tag{14}$$

The tensor $\boldsymbol{S}_d$ is defined as follows:

$$\boldsymbol{S}_d = \frac{1}{2}\left[\nabla\boldsymbol{v}\cdot\nabla\boldsymbol{v} + (\nabla\boldsymbol{v}\cdot\nabla\boldsymbol{v})^T\right] - \frac{1}{3}tr\left(\nabla\boldsymbol{v}\cdot\nabla\boldsymbol{v}\right)\boldsymbol{I}. \tag{15}$$

For LES models, the definition of the filtered heat flux in the energy equation is based on a Boussinesque approximation, where the heat flux is assumed to be proportional to the SGS viscosity. The filtered heat flux $\tilde{\boldsymbol{q}}$ in the energy equation of LES is defined as follows:

$$\tilde{\boldsymbol{q}} = -\left(\kappa + \frac{\mu_t C_p}{Pr_t}\right)\nabla\tilde{T}, \tag{16}$$

where κ is the thermal conductivity of the fluid, μ_t is the SGS viscosity as given by the respective SGS model, C_p is the specific heat, Pr_t is the turbulent Prandtl number, and $\tilde{T}$ is the filtered temperature.

The VOF multiphase model [20] was chosen to simulate and identify the interface between gas and liquid. Because of its numerical efficiency, the VOF model is suited for simulations of flows wherein each phase constitutes a large structure with a relatively small total contact area between phases [21]. In the VOF model, volume fraction is defined as the spatial distribution of each phase at a given time. It is calculated by solving a transport equation for the phase volume fraction, which is implemented in the STAR-CCM+ segregated flow model [21]. To ensure the simulation stability, the Courant–Friedrichs–Lewy (CFL) number at the liquid–gas interface should be limited to 1, and better results with a sharp resolution of the two phases are obtained with a CFL around 0.5 [22]. In this study, a second-order convection scheme implemented in the high-resolution interface capturing options was used throughout all simulations to accurately capture sharp interfaces between the two phases, namely air and water. The calculations were performed under the transient state using implicit schemes, and the Semi-Implicit Method for Pressure Linked Equations (SIMPLE) algorithm was applied for the pressure–velocity coupling to ensure an accurate and efficient solution for the unsteady Navier–Stokes equations [23]. The calculation time step dt was 0.001 s to keep the CFL number less than 0.5. According to the Star-CCM+ manuals [21], the use of implicit schemes and SIMPLE algorithm facilitates good results with higher time steps even with very high Courant numbers in VOF simulations.

2.3 Domain discretization

Fully conformal meshes were generated using polyhedral and prismal layer-meshing operations. Mesh generation was performed using the automatic meshing capabilities in Star-CCM+: surface remesher, polyhedral mesher, and prism layer mesher. The surface remesher performed surface vertex re-tessellation of the imported 3D CAD to optimize surface faces based on the target edge length and proximity refinements. The polyhedral mesher used an arbitrary polyhedral cell shape to build the core mesh. The polyhedral meshes are efficient to build because they require no more surface preparation than the equivalent tetrahedral mesh. The polyhedral meshes also contain approximately one-fifth of the cells needed for a tetrahedral mesh for a given starting surface. In the polyhedral mesher process, a tetrahedral mesh is first generated for the input surface. Second, a dualization scheme is used to create the polyhedral mesh from the underlying tetrahedral mesh. The volume growth rate controls how quickly the cell size increases with increasing distance from the surface and from refinement zones to mesh away from the zones. The

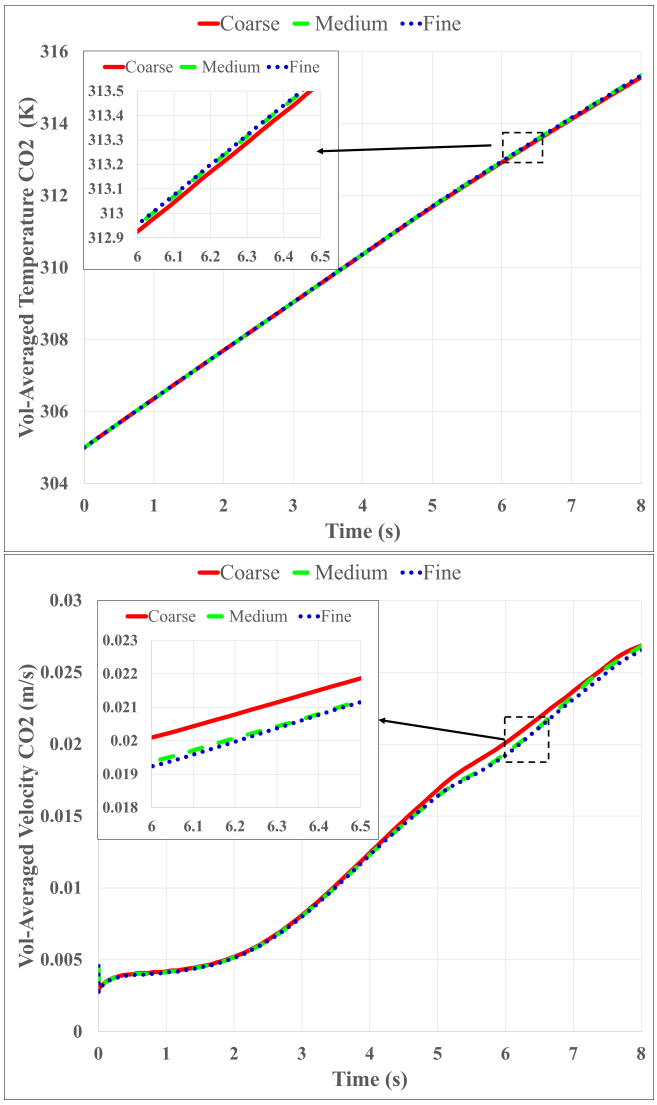

FIGURE 3: COMPARISON OF VOLUME-AVERAGED TRANSIENT TEMPERATURE AND VELOCITY OF CO_2 GAS INSIDE THE CHAMBER DURING THE COMPRESSION PROCESS FOR 8 s OBTAINED USING COARSE, MEDIUM, AND FINE MESHES.

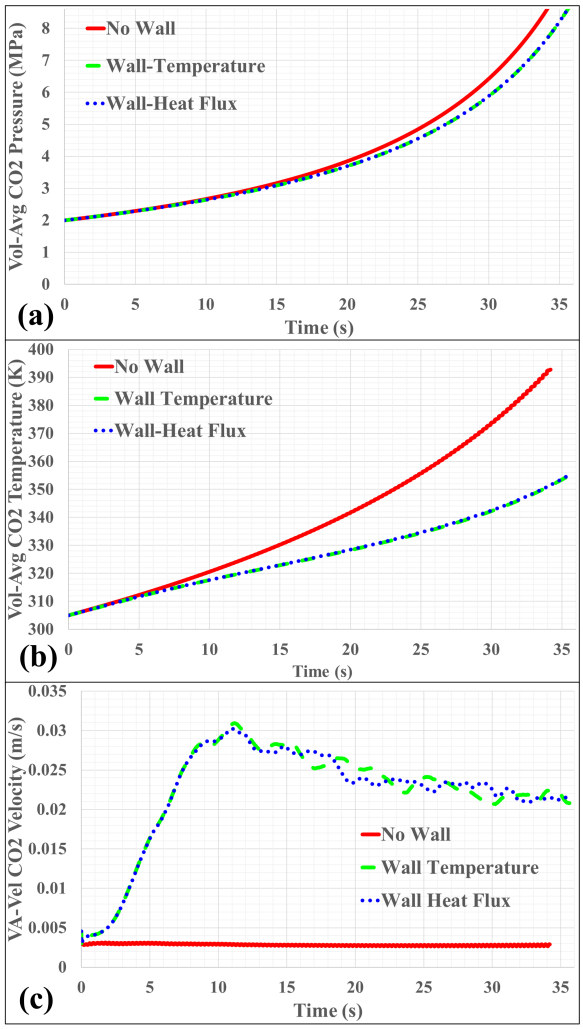

FIGURE 4: COMPARISONS OF VOLUME-AVERAGED CO_2 (a) PRESSURE, (b) TEMPERATURE, AND (c) VELOCITY OBTAINED FROM THE SIMULATIONS USING BOUNDARY CONDITIONS OF NO WALL, A WALL WITH A CONSTANT WALL TEMPERATURE, AND A WALL WITH A CONSTANT HEAT FLUX.

maximum cell size control restricts how large cells can grow. The prism layer mesher generated a subsurface to extrude a set of prismatic cells from region surfaces into the core mesh. This layer of cells is necessary to improve the accuracy of the flow solution.

Figure 2 illustrates the computational domain with two vertical planes XZ_0 and XZ_3 (i.e., side surfaces, a mid-plane XZ_2, and a horizontal plane Y_1). The solid wall is depicted as yellow, and the fluid region is depicted as blue. The computational mesh generated in the plane XZ_1, the mid-plane XZ_2, and the plane Y_1 is also shown. The sensitivity of the mesh discretization on relevant fluid flow and heat transfer quantities was investigated. Coarse, medium, and fine meshes were generated using a base cell size of 0.1905 mm with refinements to the cell sizes in the core flow and wall layers, such as target surface sizes, surface and volume grow rates, and numbers of prism layer. The resulting numbers of cells, including both fluid and solid parts for coarse, medium, and fine meshes, were 7.1×10^6, 10.9×10^6, and 18.8×10^6, respectively. The numbers of fluid cells of the coarse, medium, and fine meshes were 3.7×10^6, 5.6×10^6, and 8.7×10^6, respectively. Mesh sensitivity was evaluated by comparing the temporal evolution of quantities of interest such as volume-averaged temperature of CO_2, volume-averaged pressure of CO_2, and volume-averaged velocity of CO_2. To reduce the computational effort required for the mesh sensitivity study, numerical calculations using the coarse, medium, and fine meshes were performed for 8 s when the CO_2 pressure increased from 2 to 2.5 MPa. Figure 3 compares the volume-averaged temperature and velocity of CO_2 gas inside the chamber during the compression process for 8 s obtained using the coarse, medium, and fine meshes. The results obtained using the medium mesh of 10.9×10^6 cells and the fine mesh of 18.8×10^6 cells are similar. However, the computational time of the fine mesh was considerably longer than those of the coarse and medium meshes. Therefore, the medium mesh and

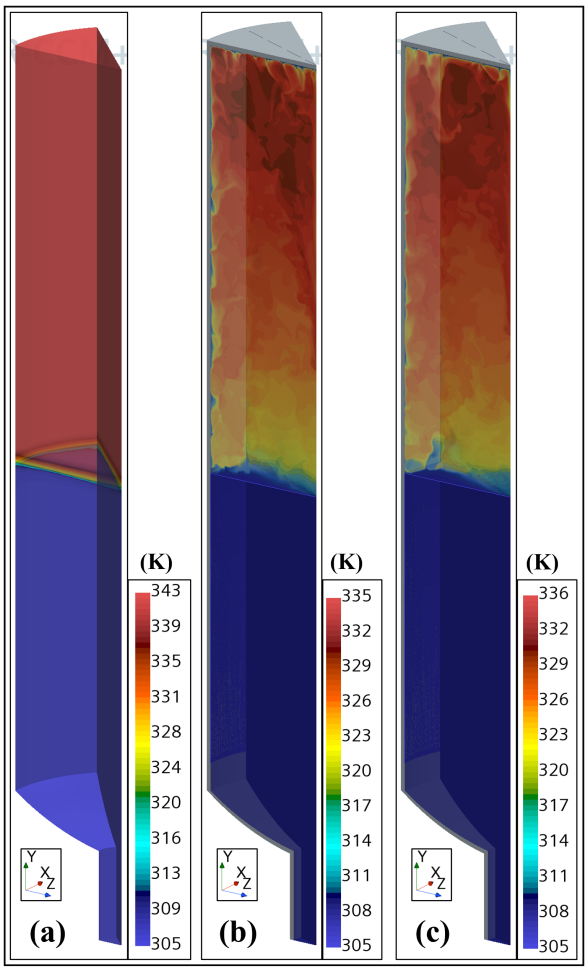

FIGURE 5: COLOR CONTOURS OF CO_2 TEMPERATURE AT t = 20 s OBTAINED FROM THE LES CALCULATIONS USING BOUNDARY CONDITIONS OF (a) NO WALL, (b) A WALL WITH A CONSTANT TEMPERATURE, AND (c) A WALL WITH A CONSTANT HEAT FLUX.

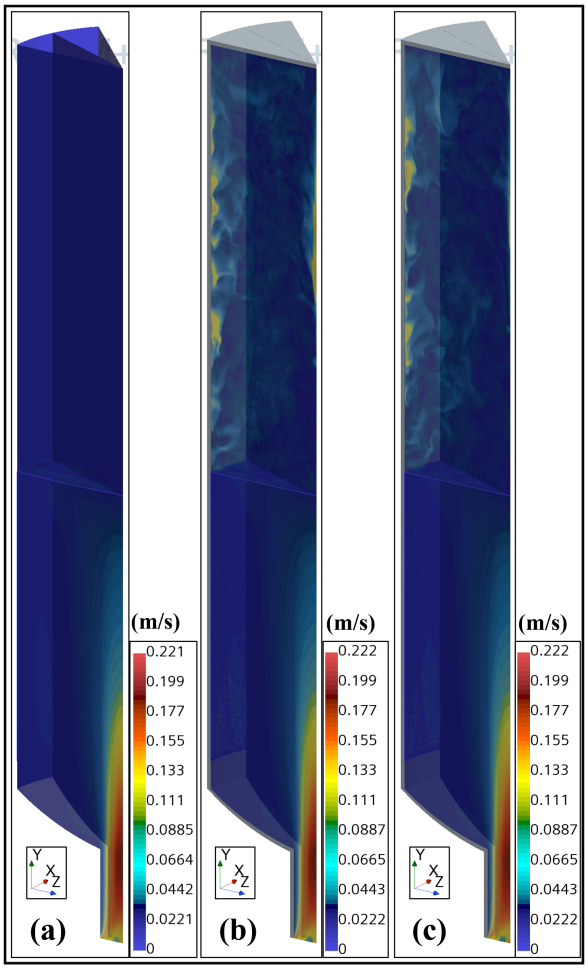

FIGURE 6: COLOR CONTOURS OF CO_2 VELOCITY MAGNITUDE AT THE INSTANT OF t = 20 s OBTAINED FROM THE LES CALCULATIONS USING BOUNDARY CONDITIONS OF (a) NO WALL, (b) A WALL WITH A CONSTANT TEMPERATURE, AND (c) A WALL WITH A CONSTANT HEAT FLUX.

corresponding meshing methodology were selected for the domain discretization of numerical investigations of a liquid piston compressor.

3. RESULTS AND DISCUSSIONS

3.1 Effects of modeling conjugate heat transfer with fluid–solid wall interactions

This subsection describes the conjugate heat transfer simulations that were performed on the numerical domain with various boundary conditions applied: no wall (only the fluid volume considered), a wall with a constant temperature of 305 K, and a wall with a constant heat flux of 60 W/m^2. Results obtained from the calculations are compared to study the effects of chamber wall on the flow and heat transfer within the chamber during the compression process.

Figure 4 shows the temporal evolution of volume-averaged pressure, temperature, and velocity of CO_2 in the compression chamber obtained from the LES calculations of a liquid piston domain corresponding the boundary conditions of no wall, a wall with a constant temperature, and a wall with a constant heat flux. Figure 4(a) shows the CO_2 gas pressure within the chamber from the beginning (i.e., when liquid PG is injected into the chamber using the bottom nozzle inlet) to the end of compression process (i.e., when the internal CO_2 pressure reaches 8.58 MPa). The LES calculation with no wall had its maximum pressure of 8.58 MPa at t = 34.1 s, whereas the LES calculations with a constant wall temperature and with a constant wall heat flux reached 8.58 MPa at t = 35.5 s.

Figure 4(b) shows that the volume-averaged temperatures of CO_2 within the compression chamber obtained from the LES calculation with no wall considered increases from 305 to 392.7 K, whereas the peaked CO_2 temperatures were at 354.9 and 355.15 K for the LES calculations with constant wall temperature and with wall heat flux, respectively. Evolution of CO_2 temperatures during the compression process is similar: a maximum temperature difference of 1.6 K occurs when the chamber wall is considered in the numerical simulations, either applying the isothermal or heat flux conditions. However, the LES calculations with no wall considered resulted in a CO_2 temperature that started to deviate from other calculated temperatures at 3.4 s: the temperature difference was 0.1 K, and maximized at 37.4 K.

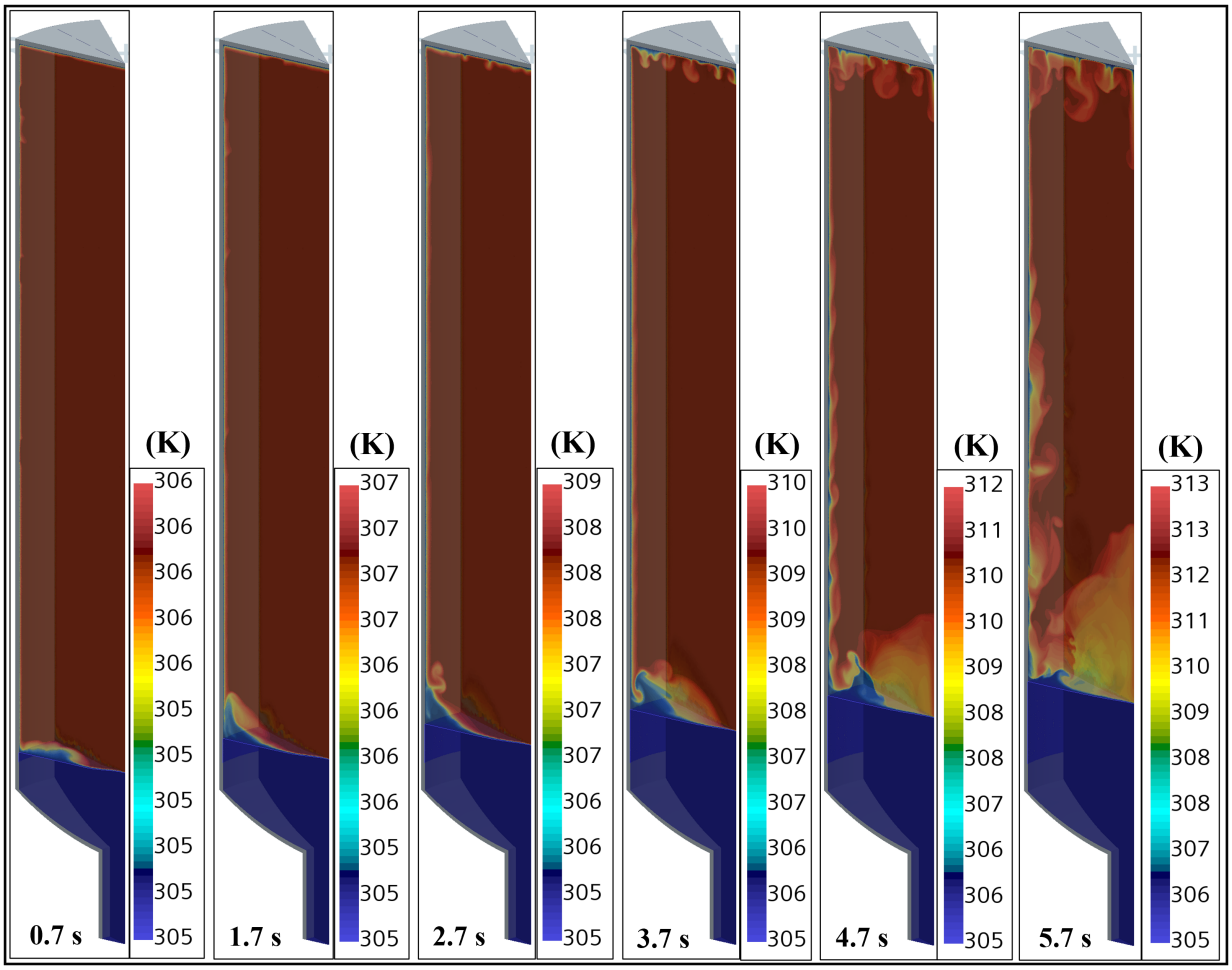

FIGURE 7: TEMPERATURE CONTOURS OF CO_2 GAS AND PG LIQUID WITHIN THE CHAMBER AT INSTANTS OF t = 0.7, 1.7, 2.7, 3.7, 4.7, AND 5.7 s. RESULTS WERE OBTAINED FROM THE LES CALCULATION OF THE COMPRESSION PROCESS USING A CONSTANT WALL HEAT FLUX CONDITION.

Comparison of volume-averaged velocity of CO_2 gas within the chamber during the compression process clearly indicates the differences of gas kinetics when the presence of a chamber wall is considered in the LES calculations. Without considering the wall, the averaged CO_2 gas velocity was between 2.6×10^{-3} and 3×10^{-3} m/s and remained stable during the compression. On the other hand, when effects of chamber wall are considered in the conjugate heat transfer calculations, the averaged CO_2 gas velocity increased from approximately 3×10^{-3} m/s at the beginning to its peak of 3×10^{-2} m/s at 11.4 s, and then gradually reduced to 2.1×10^{-2} m/s when the compression process finished.

Figures 5 and 6 illustrate the color contours of CO_2 temperature and velocity magnitudes, respectively, at the instant of $t = 20$ s obtained from the LES calculations using no wall, a wall with a constant temperature, and a wall with a constant heat flux. Figures 5(a) and 6(a) show that, when the chamber wall is excluded from the calculation, the flow and heat transfer behaviors inside the volume of the compression chamber are calm and stable. At the instant of $t = 20$ s, the injection of liquid PG into the domain through the bottom nozzle inlet slightly induced the liquid–gas interface because of the large liquid depth. In the volume of CO_2 gas, no dynamic flow patterns are observed, whereas the gas temperature increases almost linearly. The temperature is distributed uniformly in the gas volume, except in a small region near the gas–liquid interface where a large temperature gradient is observed. On the contrary, Figures 5(b–c) and 6(b–c) depict dynamic and complex patterns of temperature and velocity fields of CO_2 gas in the chamber obtained from the LES calculations using the constant wall temperature and wall heat flux. These temperature and velocity contours at the instant of $t = 20$ s are not the same. However, they reveal similar small- and large-scale flow and temperature patterns. Overall, the temperature fields in the gas volume display an increase of temperature from the gas–liquid interface to the top wall of the compression chamber. Near the chamber wall, heat transfer between the cold wall and hot CO_2 gas is indicated by the presence of a gas layer. This thin gas layer is colder than the gas in the central region, creating an internal density-driven flow region where cold (heavy) gas near the wall moves downward and hot (light) gas in the center rises upward.

Comparisons of volume-averaged pressure, temperature, and velocity with instantaneous contours of temperature and velocity

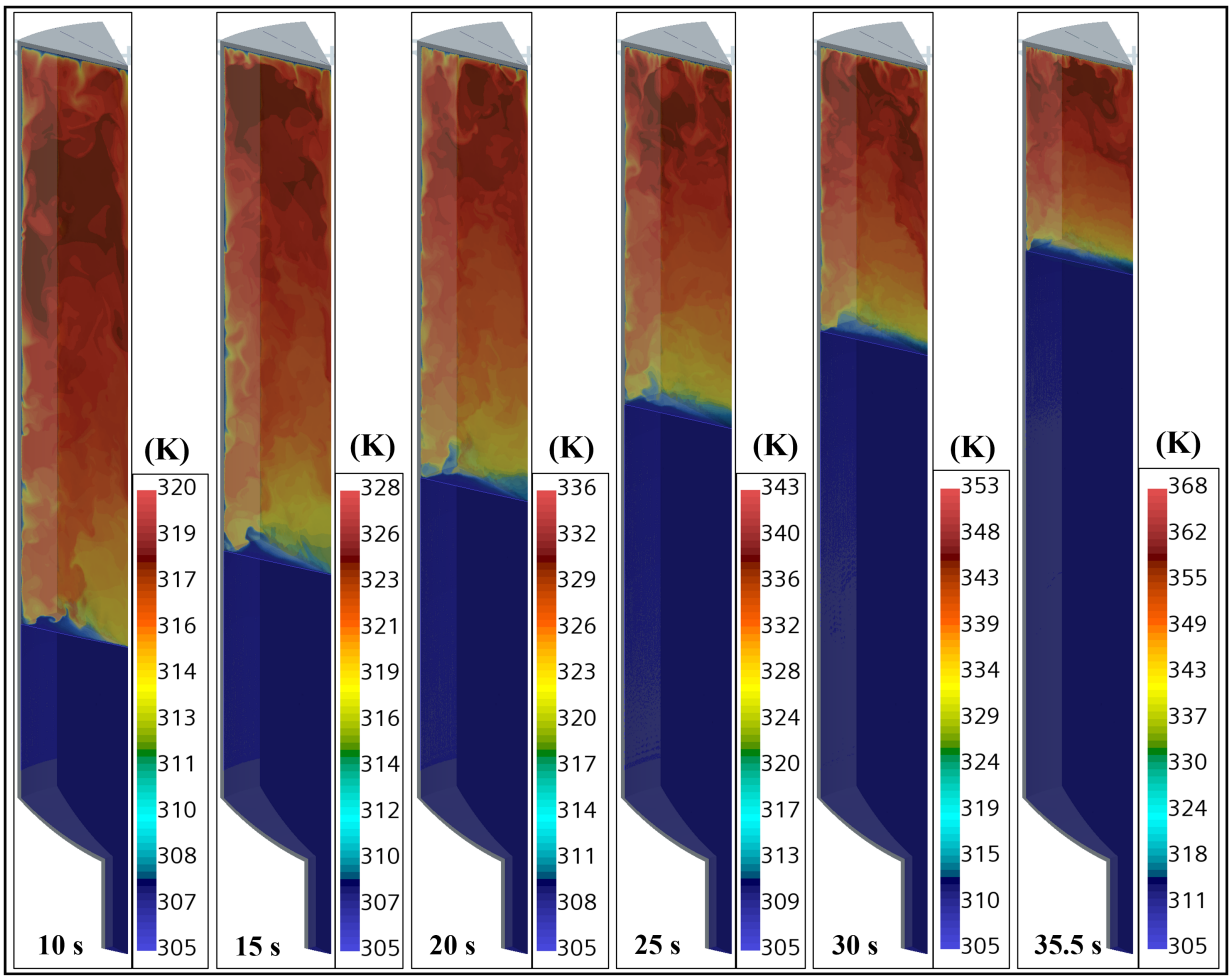

FIGURE 8: TEMPERATURE CONTOURS OF CO_2 GAS AND PG LIQUID WITHIN THE CHAMBER AT INSTANTS OF t = 10, 15, 20, 25, 30, AND 35.5 s. RESULTS WERE OBTAINED FROM THE LES CALCULATION OF THE COMPRESSION PROCESS USING A CONSTANT WALL HEAT FLUX CONDITION.

of CO_2 gas within the chamber during the compression process highlight the importance of modeling the chamber wall in the simulations of a liquid piston compressor. Therefore, results presented in the next section were obtained from the LES calculations using a constant wall heat flux.

3.2 Results of LES calculation with a constant wall heat flux condition

This subsection presents the flow and temperature fields obtained from the LES calculation of a liquid piston compressor with the injection of liquid PG from the chamber's bottom nozzle inlet at a mass flow rate of $Q_1 = 2$ L/min. The chamber was initially occupied by CO_2 gas, and initial conditions of the chamber were at a temperature of 305 K and a pressure of 2 MPa. The compression process stops when the internal pressure of chamber reaches 8.6 MPa.

The averaged temperature of CO_2 gas within the chamber is an important parameter to represent the progress of the compression process by the studied liquid piston compressor. In this study, the temperature of CO_2 gas was at $T_0 = 305$ K ($t = 0$ s) and increased to $T_{max} = 355.15$ K ($t_{max} = 35.5$ s). This temperature increase is approximately 16% and far smaller than the value of 28.7% for the adiabatic case ($T_{max} = 392.7$ K); therefore, the compression could be considered as near isothermal. In the study of a liquid piston compressor using air and water [5, 16], the authors reported a temperature increase of 11.1% and 79% for near-isothermal and adiabatic cases, respectively. The evolution of CO_2 gas temperature shown in Figure 4(b) depicts different stages of the compression process.

- Stage 1 from $t = 0$ to 4.3 s: the temperature of CO_2 gas increases almost linearly by about 1.35 K/s.
- Stage 2 from $t = 4.3$ to 24.9 s: the temperature of CO_2 gas increases slower, about 1.17 K/s.
- Stage 3 from $t = 24.9$ to 35.5 s: the temperature of CO_2 gas increases rapidly from 1.4 to 2.6 K toward the end of the compression. The temperature curve in this stage had a convex (parabolic) shape.

Different stages in the compression process of a liquid piston compressor correspond to different flow and heat transfer regimes within the chamber. Figures 7 and 8 and Figures 9 and 10 illustrate

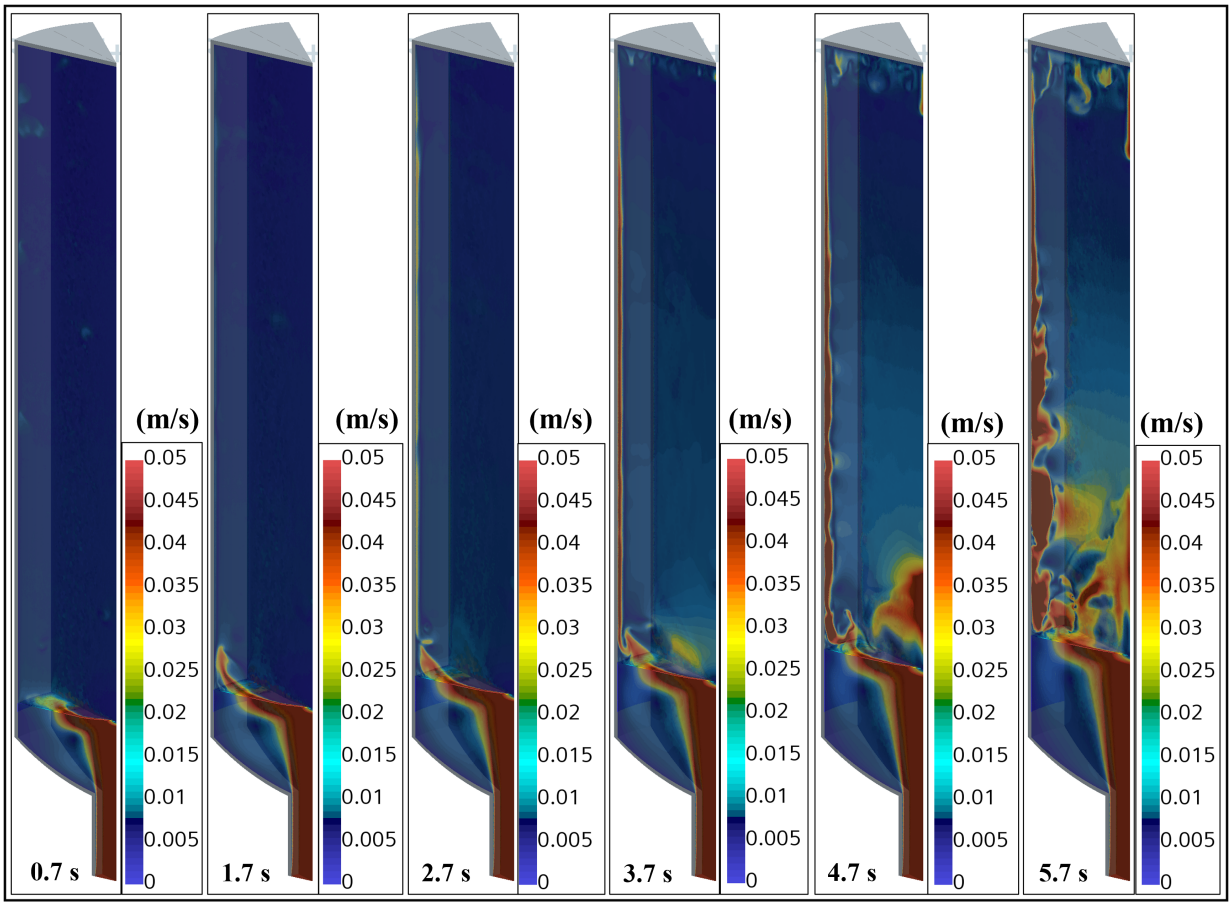

FIGURE 9: VELOCITY MAGNITUDE CONTOURS OF CO_2 GAS AND PG LIQUID WITHIN THE CHAMBER AT INSTANTS OF t = 0.7, 1.7, 2.7, 3.7, 4.7, AND 5.7 s. RESULTS WERE OBTAINED FROM THE LES CALCULATION OF THE COMPRESSION PROCESS USING A CONSTANT WALL HEAT FLUX CONDITION.

the temperature and velocity fields, respectively, evolving within the chamber during the compression process at several instants ranging from 0.7 to 35.5 s. The compression started when PG liquid was injected into the chamber through the inlet nozzle at the bottom. Because the level of liquid PG increased, temperature of CO_2 gas within the top volume started to increase. For stage 1, the interface between CO_2 gas and PG liquid was influenced, and surface waves were created: a peak occurred at the center of the chamber volume. The interface fluctuation induced a movement of CO_2 gas volume near the interface, moving toward the chamber vertical. This movement in turn initiated the heat transfer between the gas and liquid at the interface, between the gas and solid wall, and induced the mixing phenomena within the gas volume (Figures 7 and 9 show temperature and velocity fields for t = 0.7 to 4.3 s). At the end of stage 1 and transitioning into stage 2, thin layers of colder CO_2 formed along the vertical and top wall owing to the heat transfer between the solid wall and CO_2 gas. Colder gas, having greater density, was found to either move downward along the vertical wall or fall into the gas from the top wall. The thin gas layer further exchanged heat while moving along the vertical wall, expanded in width, and accelerated until it impinged upon the liquid surface. After the impingement at the interface near the vertical wall, the CO_2 gas diverged back into the gas volume and strongly enhanced the flow and heat transfer mixing inside the central gas region. The combination of these dynamic flow movements established a large circulation flow pattern within the chamber volume where the colder CO_2 gas layer moved downward along the side wall, and the warmer CO_2 gas volume moved upward in the central region. Color contours of temperature and velocity fields of t = 5.7 to 25 s in Figures 8 and 10 reveal highly dynamic flow patterns evolving within the chamber, particularly from t = 10 s, such that the gas mixing occurred within the entire internal volume of CO_2 gas. Furthermore, a temperature gradient can be observed: a colder region is near the gas–liquid interface, and a warmer region is located at the top of the chamber. In stage 3, as the liquid level increased—significantly compressing the gas and yielding higher pressure and temperature within the CO_2 gas volume—the gas temperature increased rapidly. This behavior could be explained by the reduction of heat transfer surface between the solid wall and gas layer as well as the gas volume at the top of chamber.

4. CONCLUSION

Numerical simulations of a liquid piston compressor in which the chamber fills with liquid PG from the bottom inlet to compress CO_2 were performed. The LES simulations coupled with VOF model to simulate the transient interface between liquid PG and

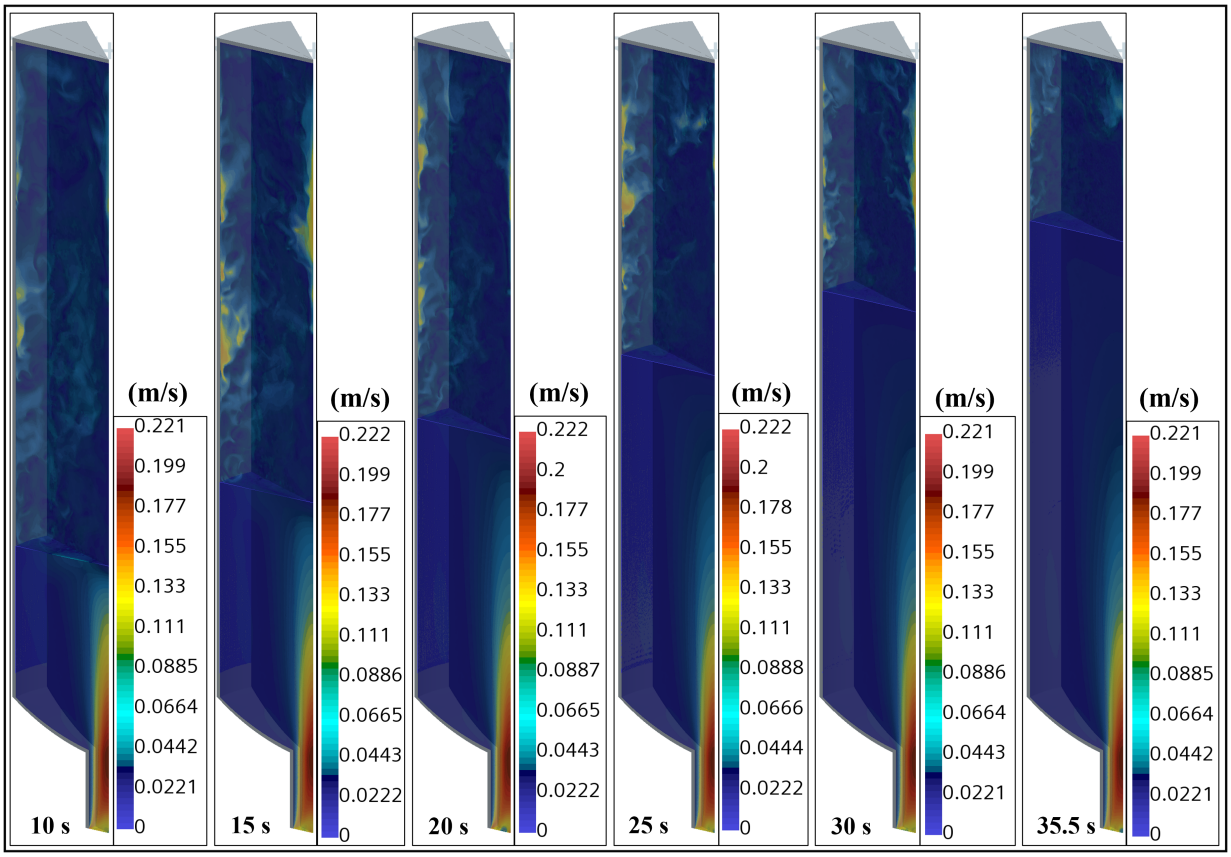

FIGURE 10: VELOCITY MAGNITUDE CONTOURS OF CO_2 GAS AND PG LIQUID WITHIN THE CHAMBER AT INSTANTS OF t = 10, 15, 20, 25, 30, AND 35.5 s. RESULTS WERE OBTAINED FROM THE LES CALCULATION OF THE COMPRESSION PROCESS USING A CONSTANT WALL HEAT FLUX CONDITION.

CO_2 gas, as well as capture the heat and mass transfer within the volume of compression chamber. In this study, effects of boundary conditions applied in the LES calculations including no wall, an adiabatic wall, and a thick wall with a heat flux subscribed were evaluated. Results obtained from the LES calculation with no wall considered have shown no dynamical flow patterns observed in the chamber, the volume-averaged temperatures of CO_2 increased from 305 to 392.7 K, and the averaged gas velocity was between 2×10^{-3} and 3×10^{-3} m/s and remained stable during the compression process. On the other hand, LES calculations with a constant wall temperature or a wall heat flux had similar increases of CO_2 temperatures (maximum difference of 1.6 K). In these cases, the peaked CO_2 velocity was 3×10^{-2} m/s at 11.4 s, and gradually reduced to 2.1×10^{-2} m/s when the compression process finished. Results of LES simulation featuring a wall heat flux revealed different stages in the compression process of liquid piston compressor and the computed temperature and velocity fields depicted dynamic and complex patterns transiently occurred in the chamber. Because of the heat transfer between the solid wall and CO_2 gas, thin layers of colder CO_2 were formed along the vertical and top walls. These layers moved downward, exchanged heat, expanded the width, and accelerated until they impinged into the liquid surface. After the impingement, the CO_2 gas layers diverged back into the gas volume and strongly enhanced mixing phenomena inside the central gas region. The LES results also revealed circulation flow patterns within the chamber volume where colder CO_2 gas layer moved downward along the side wall and warmer CO_2 gas volume moved upward in the central region. When the liquid level increased, the gas temperature increased rapidly because of the reduced heat transfer surface between the solid wall and gas layer as well as the gas volume at the top of chamber.

ACKNOWLEDGMENTS

This material is based upon work supported by the U. S. Department of Energy's Building Technologies Office under Contract No. DE-AC05-00OR22725 with UT-Battelle, LLC. The authors would like to acknowledge Mr. Antonio Bouza, Technology Manager, U.S. Department of Energy Building Technologies Office.

REFERENCES

[1] Van de Ven, James D and Li, Perry Y. "Liquid piston gas compression." *Applied Energy* Vol. 86 No. 10 (2009): pp. 2183–2191.

[2] Neu, Thibault, Solliec, Camille and dos Santos Piccoli, Bernardo. "Experimental study of convective heat transfer during liquid piston compressions applied to near isothermal underwater compressed-air energy storage." *Journal of Energy Storage* Vol. 32 (2020): p. 101827.

[3] Gerstmann, J and Hill, WS. "Isothermalization of stirling heat-actuated heat pumps using liquid pistons." *Intersociety energy conversion engineering conference. 21*: pp. 377–382. 1986.

[4] Zhou, Qian, Du, Dongmei, Lu, Chang, He, Qing and Liu, Wenyi. "A review of thermal energy storage in compressed air energy storage system." *Energy* Vol. 188 (2019): p. 115993.

[5] Gouda, El Mehdi, Benaouicha, Mustapha, Neu, Thibault, Fan, Yilin and Luo, Lingai. "Flow and heat transfer characteristics of air compression in a liquid piston for compressed air energy storage." *Energy* Vol. 254 (2022): p. 124305.

[6] Qin, Chao and Loth, Eric. "Liquid piston compression efficiency with droplet heat transfer." *Applied Energy* Vol. 114 (2014): pp. 539–550.

[7] Qin, Chao, Loth, E, Li, P, Simon, T and Van de Ven, J. "Spray-cooling concept for wind-based compressed air energy storage." *Journal of Renewable and Sustainable Snergy* Vol. 6 No. 4 (2014): p. 043125.

[8] Odukomaiya, Adewale, Abu-Heiba, Ahmad, Gluesenkamp, Kyle R, Abdelaziz, Omar, Jackson, Roderick K, Daniel, Claus, Graham, Samuel and Momen, Ayyoub M. "Thermal analysis of near-isothermal compressed gas energy storage system." *Applied Energy* Vol. 179 (2016): pp. 948–960.

[9] Patil, Vikram C, Acharya, Pinaki and Ro, Paul I. "Experimental investigation of water spray injection in liquid piston for near-isothermal compression." *Applied Energy* Vol. 259 (2020): p. 114182.

[10] Maisonnave, Océane, Moreau, Luc, Aubrée, René, Benkhoris, Mohamed-Fouad, Neu, Thibault and Guyomarc'h, David. "Optimal energy management of an underwater compressed air energy storage station using pumping systems." *Energy Conversion and Management* Vol. 165 (2018): pp. 771–782.

[11] Zhang, Chao, Saadat, Mohsen, Li, Perry Y and Simon, Terrence W. "Heat transfer in a long, thin tube section of an air compressor: an empirical correlation from CFD and a thermodynamic modeling." *ASME International Mechanical Engineering Congress and Exposition*, Vol. 45233: pp. 1601–1607. 2012. American Society of Mechanical Engineers.

[12] Zhang, Chao, Wieberdink, Jacob H, Shirazi, Farzad A, Yan, Bo, Simon, Terrence W and Li, Perry Y. "Numerical investigation of metal-foam filled liquid piston compressor using a two-energy equation formulation based on experimentally validated models." *ASME International Mechanical Engineering Congress and Exposition*, Vol. 56352: p. V08BT09A045. 2013. American Society of Mechanical Engineers.

[13] Schober, M, Deichsel, M and Schlucker, E. "Computational fluid dynamics simulation and experimental validation of heat transfer in liquid piston compressors." *12th International Conference on Heat Transfer. Fluid Mechanics and Thermodynamics, HEFAT*: pp. 511–516. 2016.

[14] Shah, Ramesh K and Sekulic, Dusan P. *Fundamentals of heat exchanger design*. John Wiley & Sons (2003).

[15] Tuhovcak, Jan, Hejčík, Jiří and Jícha, Miroslav. "Modelling fluid flow in a reciprocating compressor." *EPJ Web of Conferences*, Vol. 92: p. 02100. 2015. EDP Sciences.

[16] Gouda, EM, Benaouicha, M, Neu, T, Vergnol, P, Yilin, F and Luo, L. "2D versus 3D numerical modeling of flow and heat transfer in a liquid piston air compressor." *ICNAAM 2021 19th International Conference Of Numerical Analysis And Applied Mathematics, Rhodes, Greece*. 2021.

[17] Muzaferija, Samir. "Computation of free surface flows using interface-tracking and interface-capturing methods." *Nonlinear water-wave interaction. Computational Mechanics, Southampton* (1998).

[18] Smagorinsky, Joseph. "General circulation experiments with the primitive equations: I. The basic experiment." *Monthly weather review* Vol. 91 No. 3 (1963): pp. 99–164.

[19] Nicoud, Franck and Ducros, Frédéric. "Subgrid-scale stress modelling based on the square of the velocity gradient tensor." *Flow, turbulence and Combustion* Vol. 62 No. 3 (1999): pp. 183–200.

[20] Hirt, Cyril W and Nichols, Billy D. "Volume of fluid (VOF) method for the dynamics of free boundaries." *Journal of Computational Physics* Vol. 39 No. 1 (1981): pp. 201–225.

[21] Guide, User. "StarCCM+ version 2021.1." *SIEMENS simcenter* (2021).

[22] Connell, Ken O and Cashman, Andrew. "Development of a numerical wave tank with reduced discretization error." *2016 International Conference on Electrical, Electronics, and Optimization Techniques (ICEEOT)*: pp. 3008–3012. 2016. IEEE.

[23] Ferziger, Joel H, Perić, Milovan and Street, Robert L. *Computational methods for fluid dynamics*. Vol. 3. Springer (2002).